Numerical investigations of rotational effects on boundary-layer instabilities on the Z49 open rotor model

Alexander Theiss, Stefan Hein, Lucas Pascal, Julien Cliquet

Numerical investigations of rotational effects on boundary-layer instabilities on the Z49 open rotor model

Alexander Theiss* and Stefan Hein†
German Aerospace Center, Institute of Aerodynamics and Flow Technology, Göttingen, 37073, Germany

Lucas Pascal‡
ONERA–University of Toulouse, F-31055 Toulouse, France

Julien Cliquet§
Airbus Operations SAS, Toulouse, France

Spatial linear stability analyses are performed in order to study laminar-turbulent transition in the boundary layer on the Z49 rotor, rotating in a $Ma_\infty = 0.75$ freestream. In a rotating reference frame, terms corresponding to Coriolis and centrifugal forces appear in the linearized disturbance equations. However, the effect of these rotational terms on the stability of boundary layers is only partially understood. The rotational terms' impact on the transition mechanisms is studied by neglecting or considering rotation in the linear local stability and parabolized stability equations. The present results show that rotation hardly affects the instability characteristics of Tollmien-Schlichting waves. On the other hand, rotation destabilizes the cross-flow instabilities, but not enough to trigger cross-flow-dominated transition at the investigated operating condition.

I. Nomenclature

Roman symbols:

f	=	frequency, Hz
i	=	imaginary unit, $i = \sqrt{-1}$
i, j, k	=	structured grid indices
K	=	disturbance kinetic energy
$\mathbf{k}$	=	wave vector
Ma	=	Mach number
N	=	logarithmic amplification factor, N-factor
p	=	pressure, Pa
$\bar{\mathbf{q}}$	=	basic flow vector
$\tilde{\mathbf{q}}$	=	unsteady perturbation vector
$\hat{\mathbf{q}}$	=	vector of amplitude functions
R	=	rotor radius, m
r	=	local radius, m
Re_{δ_1}	=	Reynolds number based on displacement thickness
s	=	arc length along surface, m
T	=	temperature, K
t	=	time, s
$\mathbf{U}$	=	velocity vector
U, V, W	=	velocity components along streamwise, azimuthal, and wall-normal directions, m/s
$\mathbf{x}$	=	vector between the rotation vector and a considered point

*Research Scientist, Department of High Speed Configurations, DLR Göttingen, alexander.theiss@dlr.de
†Research Scientist, Department of High Speed Configurations, DLR Göttingen
‡Research Scientist, Multi-Physics and Energetics Department
§Engineer

x, y, z = Cartesian coordinates
x_1, x_2, x_3 = streamwise, azimuthal, and wall-normal coordinates

Greek symbols:

α = disturbance wavenumber in the streamwise direction, 1/m
α_i = imaginary part of the complex-valued streamwise wavenumber, 1/m
α_r = real part of the complex-valued streamwise wavenumber, 1/m
β = wavenumber of the disturbance in the azimuthal direction, 1/m
Ψ = wave angle, deg
$\mathbf{\Omega}$ = rotation vector
ω = angular frequency, Hz
ρ = density, Kg/m^3
σ = spatial disturbance growth rate, 1/m

Subscripts:

$()_\infty$ = freestream value
$()_{cr}$ = critical value where transition occurs
$()_e$ = value at the boundary-layer edge
$()_{max}$ = maximum value

Superscripts:

$\bar{()}$ = time-averaged quantity
$\tilde{()}$ = disturbance quantity
$\hat{()}$ = amplitude function

II. Introduction

The state of the boundary layer (i.e., laminar, transitional, or turbulent) significantly affects the skin friction drag and the thermal load of objects moving in the air. A longer laminar run length can thus positively affect the overall performance, e.g., via less fuel consumption during aircraft flight, a higher energy yield of wind turbines, or lower engine power requirements in propeller-driven aircraft.

Flows over rotating geometries are encountered in a great number of aeronautical applications (e.g. propellers, rotors, wind turbines, helicopter blades, etc.). In most of these applications, the configuration exhibits rotating blades of some sort. The laminar to turbulent transition on rotor blades has been studied experimentally for decades, for instance see the publication of McCroskey [1] for helicopter blades or the more recent papers of Schülein et al. [2] and Lang et al. [3]. It is well-known that the laminar-turbulent transition is postponed in comparison with a non-rotating configuration (see Ref. [4] for a propeller configuration and Refs. [5, 6] for more recent results on wind turbines). A physical interpretation is that the radial velocity component generated by the centrifugal force leads to an azimuthal Coriolis force which acts as a favorable pressure gradient and thus stabilizes the boundary layer. Moreover, the centrifugal force tends to make the boundary layer thinner in comparison with non-rotating cases. The main consequence is a delayed separation on the suction side.

However, transition prediction on rotating geometries is still a challenging task due to, among other things, the many possible transition mechanisms, such as laminar separation bubbles, attachment line transition, Görtler vortices, Tollmien-Schlichting waves, cross-flow vortices, or bypass transition. On the one hand, fully empirical transition prediction methods are used (e.g., see Ref. [7]) utilizing approximate integral and local boundary-layer quantities to check for transition criteria based on stationary wind-tunnel tests. On the other hand, the more physics-based semi-empirical e^N method is also employed (e.g., see Ref. [8]). The e^N method was originally developed by Smith & Gamberoni [9] and van Ingen [10] and is based on linear stability theory (LST). The growth of primary instabilities in the boundary layer (e.g., Tollmien-Schlichting or cross-flow waves) is captured by the e^N value, which represents the amplification ratio with respect to the initial wave amplitude. Transition is assumed to occur when a critical amplification factor N_{cr} is reached. In the LST, the initial amplitude of the primary instability is usually unknown and the value of N_{cr} has to be calibrated by, e.g., experimentally obtained transition locations.

Linear stability computations in the rotating frame based on local, parallel theory have been performed with laminar basic flows stemming from boundary-layer methods or similarity solutions for simple geometries: disks [11, 12], cones [13], and flat plates [14]. However, little is known about the impact of rotation on the transition mechanisms on industry relevant rotating geometries (e.g., rotor blades) where the three-dimensional basic flow is usually computed with a CFD code.

Lang et al.[3] and Weiss et al. [8] used the e^N method to predict the transition on a helicopter rotor blade, and Gross et al. [15] performed stability analyses for the boundary layer on a wind turbine blade. But, in those studies, the additional terms stemming from the centrifugal and Coriolis accelerations were not included in the stability equations. To the authors' knowledge, the studies of Martinez Hernandez et al. [16] and Pascal et al. [17] are so far the only ones that considered rotational forces in the instability analysis of rotating blade boundary layers. Martinez Hernandez et al. [16] report that on the investigated NM80 wind turbine rotor, the rotational forces may have a stabilizing effect on boundary-layer transition. In contrast, Pascal et al. [17] report that the inclusion of the rotational terms in the linear stability equations hardly modifies the Tollmien-Schlichting waves, while the cross-flow instability is destabilized on the considered fan blade.

The effects of rotation on the stability of boundary layers are still only partially understood. One of the main open questions is concerned with the nature of the laminar-turbulent transition. Does rotation add new kinds of instabilities, or does it only alter transition mechanisms already existing in non-rotating cases? Yecko & Rossi [18] and Dechamps & Hein [19] studied two-dimensional flow over a flat plate under the effect of rotation and observed that rotation destabilizes the flow and generates a new kind of instability in addition to the standard Tollmien-Schlichting instability. Pascal et al. [17], on the other hand, observed no new kind of instability; the rotational effect causes destabilization of already existing cross-flow instabilities.

This paper represents a numerical study on rotational effects on the instability characteristics of primary instability modes on a rotor blade at $Ma_\infty = 0.75$. The main objective of the current work is to contribute to a better understanding of rotational effects on the stability of boundary layers located on industrial relevant geometries. Therefore, linear local instability theory is used to study the impact of the additional Coriolis and centrifugal acceleration terms present in a rotating reference frame on the instability properties. In particular, the influence of rotational effects on the different primary instability modes (i.e., Tollmien-Schlichting waves and cross-flow instabilities) is investigated in more detail. Moreover, the impact of the distance to the axis of rotation is also considered. Finally, the influence of rotational effects is examined considering non-local instability theory. The insights gained in this study should help assess the extent to which the additional acceleration terms in a rotating reference frame need to be considered in an instability-based transition prediction framework. Moreover, this work will further help to clarify whether rotation adds new kinds of instabilities or merely alters existing transition mechanisms present in non-rotating cases.

III. Theory

To study the effect of rotation on the primary instability modes, the DLR in-house parabolized stability equations (PSE) based code NOLOT has previously been extended to rotating reference frames [19]. The effect of the rotation vector $\mathbf{\Omega}$ is taken into account via terms corresponding to the Coriolis $2\rho\mathbf{\Omega} \times \mathbf{U}$ and centrifugal $\rho\mathbf{\Omega} \times (\mathbf{\Omega} \times \mathbf{r})$ forces ($\mathbf{r}$ is the vector between the rotation vector and the considered point). The reader is referred to the work of Hein et al. [20] for the detailed implementation of the stability equations for boundary layers in NOLOT.

The laminar basic flow $\mathbf{q}$ can be decomposed into a steady mean flow $\bar{\mathbf{q}}$ and an unsteady perturbation component $\tilde{\mathbf{q}}$: $\mathbf{q} = \bar{\mathbf{q}} + \tilde{\mathbf{q}}$. The normal-mode solution is assumed for the disturbance quantities and the amplitude functions have a slow variation along the streamwise direction. The perturbations on the velocity field ($\tilde{u}$, $\tilde{v}$, $\tilde{w}$) the temperature $\tilde{T}$ and the density $\tilde{\rho}$ take the following form for $\tilde{\mathbf{q}} = \left(\tilde{\rho},\ \tilde{u},\ \tilde{v},\ \tilde{w},\ \tilde{T}\right)^T$:

$$\tilde{q}\left(x_1, x_2, x_3, t\right) = \hat{q}\left(x_1, x_3\right) \exp\left(i\left(\int \alpha(x_1)\mathrm{d}x_1 + \beta x_2 - \omega t\right)\right). \tag{1}$$

Throughout this paper, the spatial stability theory is employed. Hence, ω is the real-valued angular frequency and the streamwise wave number $\alpha = \alpha_r + i\alpha_i$ is a complex number. The streamwise and spanwise components of the wavevector $\mathbf{k}$ are the real part of α ($= \alpha_r$) and $\beta = \beta_r$. The angle between the wavevector $\mathbf{k}$ and the x_1-direction is equal to $\Psi = \tan^{-1}(\beta/\alpha_r)$.

In the local stability theory (LST), where also a parallel mean flow is assumed, the amplification rate along the x_1-direction σ is defined as $\sigma = -\alpha_i$. In contrast, in the nonlocal stability theory – utilized via the parabolized stability equations (PSE) – the spatial growth rate is defined as $\sigma = -\alpha_i + \partial \ln(\sqrt{K})/\partial x_1$ with K being the disturbance kinetic energy.

IV. Laminar basic flow

The model of interest belongs to a scaled version of the Z49 open rotor configuration with a front rotor radius of $R = 0.4295$ m rotating at 4503.27 rounds per minute. The freestream and open rotor operating conditions correspond to a typical nominal cruise condition and are as follows: $Ma_\infty = 0.75$, $T_\infty = 283.95$ K, and $p_\infty = 61537.45$ Pa.

The laminar basic flow, on which the linear instability analyses are performed, corresponds to the laminar region of a RANS computation. In this paper, the analyses of both laminar mean flow properties and primary mode instability characteristics are limited to the front rotor blade. In particular, the main part of the investigations is devoted to the rotor suction side due to a larger region of laminar flow (see Fig. 1). Moreover, results are solely presented for the laminar-flagged flow regions depicted in Fig. 1.

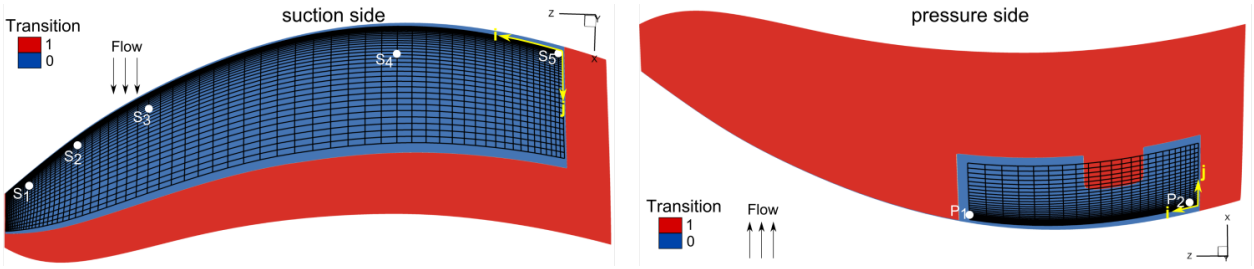

(a) **(b)**

Fig. 1 Distribution of laminar and turbulent flow regions on the front rotor blade; (a) suction side and (b) pressure side.

The laminar flow data are contained within a structured grid. The grid on the rotor's suction side has 68 points in i-direction (corresponding to the radial direction), 34 Points in j-direction (approximately corresponding to the flow direction), and 200 points in k-direction (the wall-normal direction). The laminar grid on the rotor's pressure side consists of $i, j, k = 24 \times 28 \times 200$ points, with a turbulent-flagged region ranging from $i = 11{:}16$, $j = 21{:}28$, and $k = 1{:}200$ (cf. Fig. 1(b)).

To study the impact of the distance to the axis of rotation, five positions at different radial distances are examined in more detail on the rotor suction side (points S_1–S_5 depicted in Figs. 1,2,3, and 13) and two locations on the rotor's pressure side (points P_1 and P_2 depicted in Figs. 1,2,3, and 13). The considered locations correspond to surface grid points, and their grid indices, along with characteristic boundary-layer information, are given in Table 1 for points S_1–S_5 and Table 2 for points P_1 and P_2.

Figure 2 depicts the isentropic Mach number distribution on the rotor's suction (Fig. 2(a)) and pressure side (Fig. 2(b)). In the laminar region studied, the flow around the rotor is transonic, and the Mach number increases with distance from the axis of rotation. Tollmien-Schlichting waves are preferentially amplified in an unfavorable pressure gradient environment. The largest area with an adverse pressure gradient is located in the hub area, so it can be anticipated that the Tollmien-Schlichting instabilities (TSI) are most strongly amplified there.

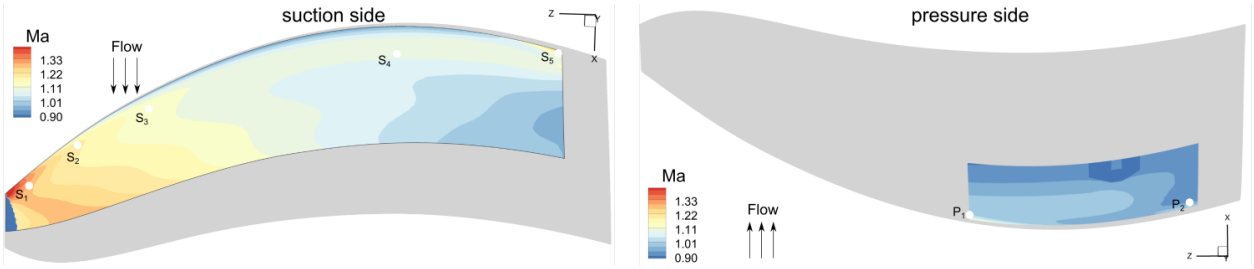

(a) **(b)**

Fig. 2 Isentropic Mach number distribution on (a) the rotor's suction side and (b) the rotor's pressure side.

Cross-flow instabilities (CFI) on the other hand can be amplified in three-dimensional boundary layers exhibiting an inflection point in the cross-flow velocity component. An indicator for the presence of amplified CFI is the ratio of

maximum cross-flow velocity to boundary layer-edge velocity V_{max}/U_e, which is shown in Fig. 3. There is a radially extending region of increased cross-flow velocity containing the points S_2 and S_3 where CFI could be amplified on the suction side leading-edge area. However, the other points also feature high cross-flow velocities, so that the CFI could be amplified there as well (see V_{max}/U_e in Tables 1 and 2).

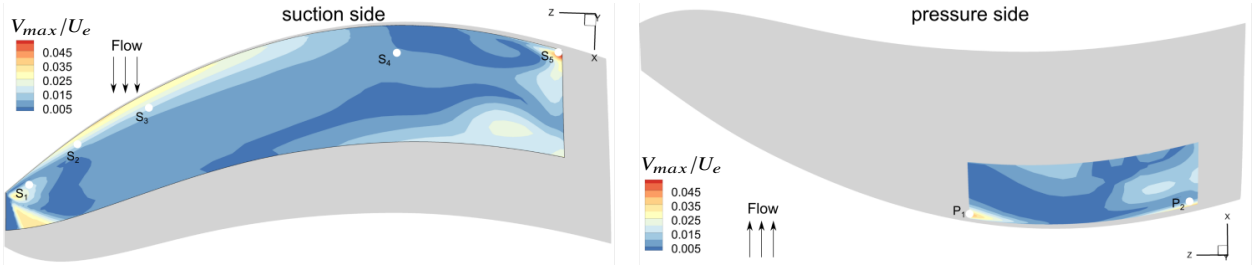

(a) **(b)**

Fig. 3 Spatial distribution of the maximum cross-flow velocity non-dimensionalized with the magnitude of the boundary-layer edge velocity for (a) the rotor´s suction side and (b) its pressure side.

Table 1 Overview of the examined points on the rotor suction side.

Point	Grid i-index	Grid j-index	r/R	Re_{δ_1}	V_{max}/U_e	Ma
S_1	55	20	0.970	864.66	0.0172	1.277
S_2	44	14	0.916	635.59	0.0142	1.195
S_3	36	16	0.840	817.74	0.0156	1.135
S_4	20	22	0.576	1333.81	0.0057	1.053
S_5	2	5	0.405	765.52	0.03041	1.131

Table 2 Overview of the examined points on the rotor pressure side.

Point	Grid i-index	Grid j-index	r/R	Re_{δ_1}	V_{max}/U_e	Ma
P_1	24	8	0.647	789.07	0.0407	1.026
P_2	3	7	0.409	615.73	0.0102	0.935

V. Impact of rotational effects on the primary instability modes

This section investigates the impact of the additional rotational terms in the stability equations on the properties of the primary linear instabilities on the Z49 rotor blade. The effect of the rotational terms is addressed by presenting the results of two sets of computations, one in which the rotation terms are neglected and one in which they are considered. First, a cross-validation of the instability results is presented for point S_4 in Sec. V.A. Subsequently, the local instability results for the considered points are given in Sec. V.B for the rotor's suction and pressure side. Finally, a global assessment of the rotational effects is given in Sec. V.C in terms of N-factor results employing both local (LST) and nonlocal (PSE) instability theory.

A. Comparison between Onera and DLR results

At DLR, there exists limited experience for instability analyses on industrially relevant geometries in a rotating reference frame. Therefore, before investigating the influence of the rotational terms on the primary instability properties in more detail, the laminar basic flow preparation approach is first verified by comparing the instability results for the T-S wave at point S_4 with the data obtained with Onera's MAMOUT [21] code. The cross-validation in terms of isocontours of the spatial growth rate in the frequency spanwise wavenumber parameter space (the $f-\beta$ plane) is shown in Fig. 4(a), whereas Fig. 4(b) shows the amplification rate as a function of disturbance frequency for selected spanwise wavenumbers for better comparability. Note that the rotational terms were not included in the instability analysis.

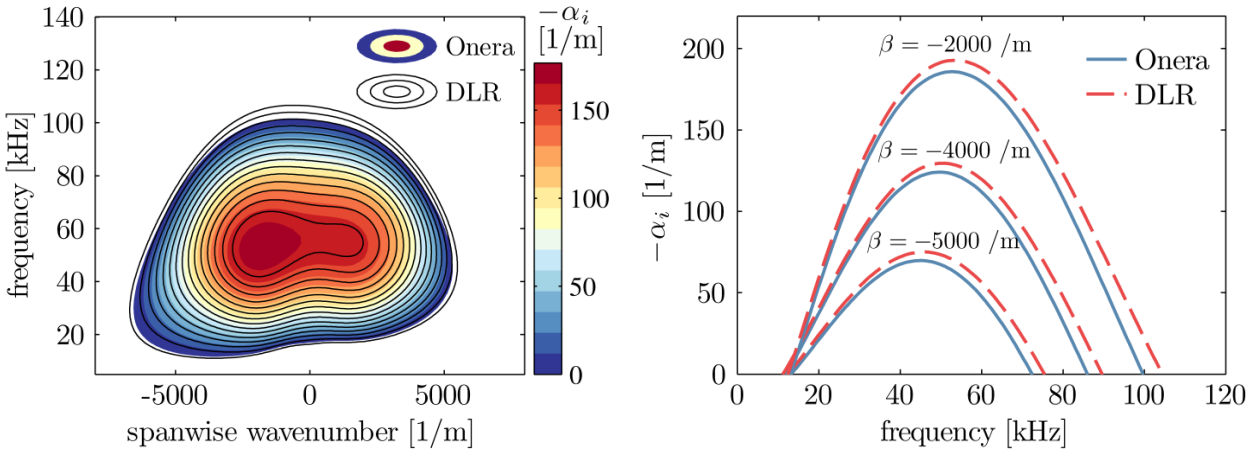

(a) **(b)**

Fig. 4 Comparison of the spatial growth rate computed by Onera and DLR for point S_4; (a) Contours of the spatial growth rate in the $f-\beta$ plane and (b) spatial growth rate as a function of disturbance frequency for selected spanwise wavenumbers.

Overall there is a good agreement between the DLR and Onera results in terms of the amplified frequency band, relevant spanwise wavenumbers, and the respective amplification rate $-\alpha_i$. The slight discrepancy between the Onera and DLR results is likely caused by the heavy amount of pre-processing necessary to prepare the CFD solution for the subsequent instability analysis. The pre-processing comprises the following steps: (i) transformation of the velocity field into the rotating frame of references, (ii) interpolation of the CFD solution onto a wall-normal grid to extract the boundary-layer profiles, and (iii) computation of all basic flow derivatives (preferably with a high-order method).

The final paper will contain a more thorough cross-comparison study, also including the rotational effects.

B. Spatial growth rate on rotor suction and pressure side

In this subsection, the effect of the rotational terms on the local instability properties is studied in detail for the selected locations given in Tables 1 and 2. For all presented results, the azimuthal direction points towards the rotational axis (negative z-direction). Furthermore, all instability results presented in this subsection are displayed as contour levels of the spatial growth rate in the $f-\beta$ plane (subfigures (a) in Figs. 5–7,9–12). The contour surfaces stand for the primary instability mode computed without the rotational terms, whereas the isolines stand for the results including the rotational effects. The subfigures (b) in Figs. 5-7,9–12 show supplementary spatial growth rates as a function of disturbance frequency for selected spanwise wavenumbers.

1. Rotor suction side

Figures 5–10 show the instability results for the selected points on the rotor suction side. The depicted amplification rates for the points S_1, S_4, and S_5 (Figs. 5, 9, and 10) belong to a Tollmien-Schlichting instability. At the location S_2 (Fig. 6), the cross-flow instability is amplified, whereas at S_3 (Figs. 7 and 8), both T-S waves and cross-flow instabilities are unstable.

The highest growth rates for the T-S unstable considered points (S_1, S_4, and S_5) are reached in the hub area at point

S_5. Considering the rotational effects in the LST has no impact on the T-S instability characteristics since just about all results are on line width with the data without rotational effects. There is a slightly destabilizing effect of the rotational terms on the T-S instability at higher spanwise wavenumbers at point S_1. This slight destabilizing effect could be linked to the impact of the distance to the rotational axis since point S_1 is located closest to the blade tip region.

On the other hand, there is an observable effect of the rotational terms on the amplification of cross-flow instabilities at point S_2 (see Fig. 6). The inclusion of the Coriolis and centrifugal forces in the instability analysis lead to a stronger amplification of the cross-flow instability accompanied by a shift of the unstable region in the $f-\beta$ plane to lower frequencies and higher absolute values of the spanwise wavenumber.

Of particular interest are also the instability results for the point S_3, where both the T-S wave and the cross-flow instability are amplified. In accordance with the findings for the other considered points, where solely one instability type is amplified (T-S waves at points S_1, S_4, and S_5 and CFI at point S_2), the instability characteristics of the T-S wave remain unchanged, whereas the parameter space of the amplified CFI is again slightly altered. A possible reason for the different effects of rotation on T-S waves and cross-flow instabilities could be due to the wave propagation direction. In the study of Dechamps & Hein [19], it is shown that instabilities propagating normal to the flow direction are most affected by rotation, and that influence increases with rotation speed. Figure 8 depicts the spatial growth rate already shown in Fig. 7(a) as a function of wave angle instead of wavenumber. The CFI propagate almost transverse to the main flow direction, whereas TSI are amplified at considerably lower wave angles.

In summary, it can be concluded that the inclusion of the rotational terms in the instability analysis hardly affects the instability characteristics of the Tollmien-Schlichting waves. On the other hand, cross-flow instabilities are destabilized by the effect of the rotational terms. However, the maximum growth rate of the CFI on the considered Z49 geometry and at the investigated rotation speed is more than an order of magnitude lower than the growth rates of the TSI. The fact that the growth rate of the Tollmien-Schlichting waves is hardly altered when including the rotational effects is in line with the findings of Dechamps & Hein [19] for a rotating Blasius boundary-layer profile and with the recent results of Pascal et al. [17] for the boundary layer on a rotating fan blade with incoming flow. Furthermore, the destabilizing effect of rotation on the cross-flow instability is also in agreement with the findings of Pascal et al. [17] and with the work of Garrett et al. [13] and Hussain et al. [12]. The author of Refs. [13] and [12] performed linear stability analyses for the flow on a broad rotating cone (Ref. [13]) and over a rotating disk (Ref. [12]) in an enforced axial flow. In those studies, the cross-flow instability amplification rate increased with the ratio of rotation speed over incoming flow velocity.

Unlike in the case of the rotating Blasius profile studied by Dechamps & Hein [19], where a new type of instability occurred at high spanwise wavenumbers and considerably smaller values of α_r, no new additional rotational instabilities were discovered in this work. However, this wavenumber combination is characteristic of cross-flow instabilities, which are already amplified on the Z49 rotor even when the rotational terms are not considered.

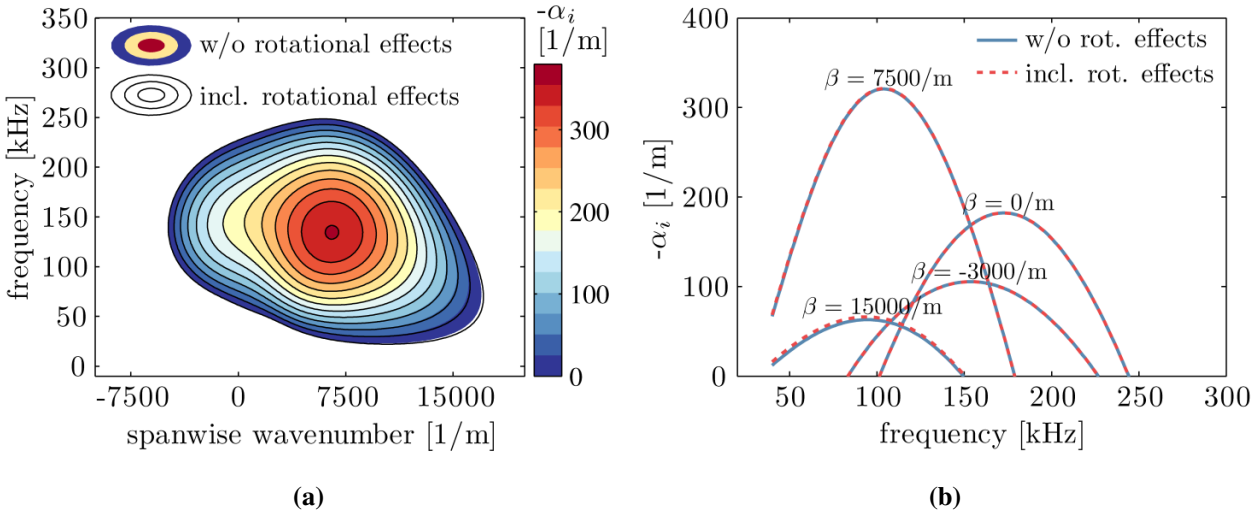

(a) **(b)**

Fig. 5 Impact of rotational effects on the spatial growth rate, $-\alpha_i$, of a Tollmien-Schlichting wave at point S_1; (a) contours of the spatial growth rate in the $f-\beta$ plane and (b) spatial growth rate as a function of disturbance frequency for selected spanwise wavenumbers.

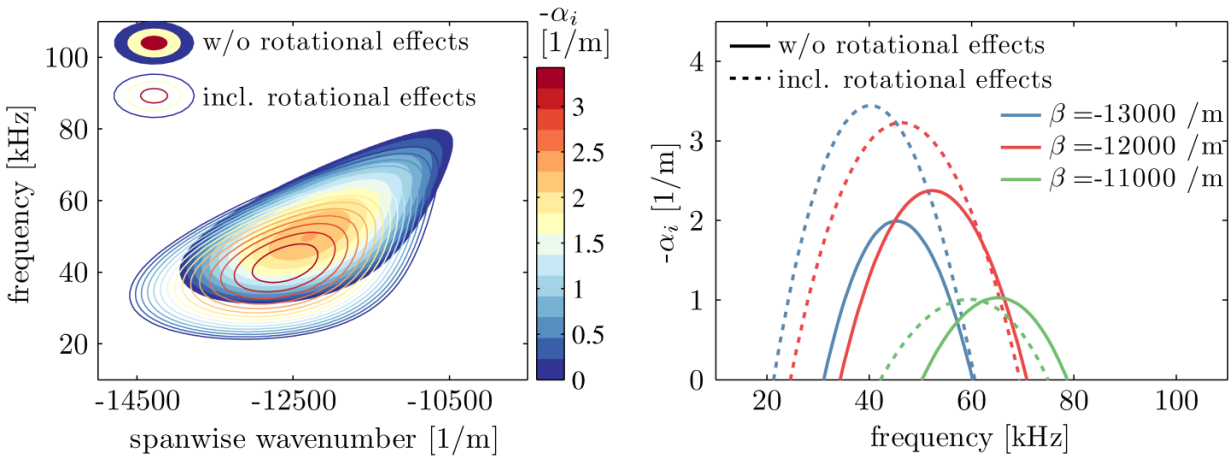

(a) **(b)**

Fig. 6 Impact of rotational effects on the spatial growth rate, $-\alpha_i$, of a cross-flow instability at point S_2; (a,b) as labeled in Fig. 5.

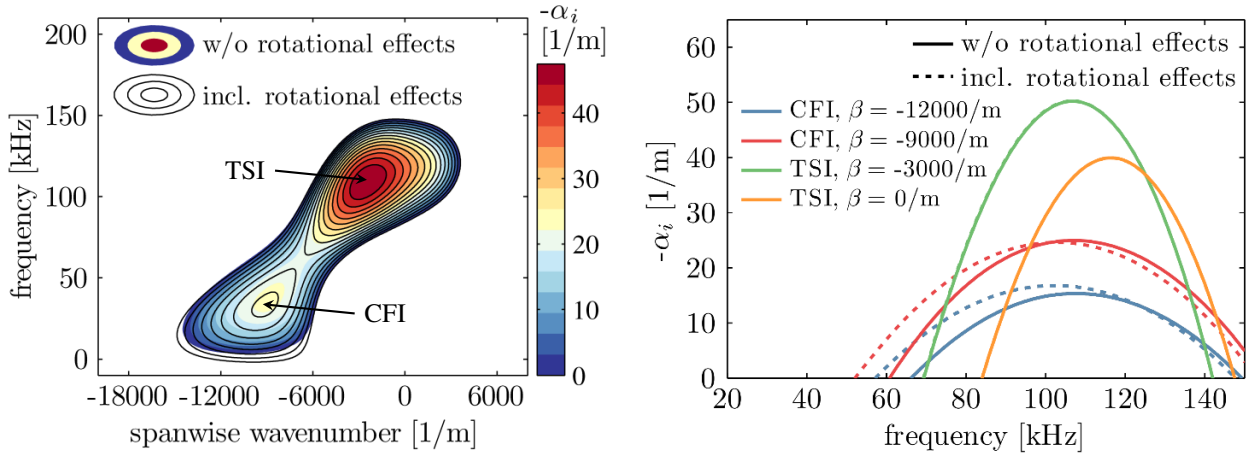

(a) **(b)**

Fig. 7 Impact of rotational effects on the spatial growth rate, $-\alpha_i$, of a Tollmien-Schlichting and cross-flow instability at point S_3;(a,b) as labeled in Fig. 5.

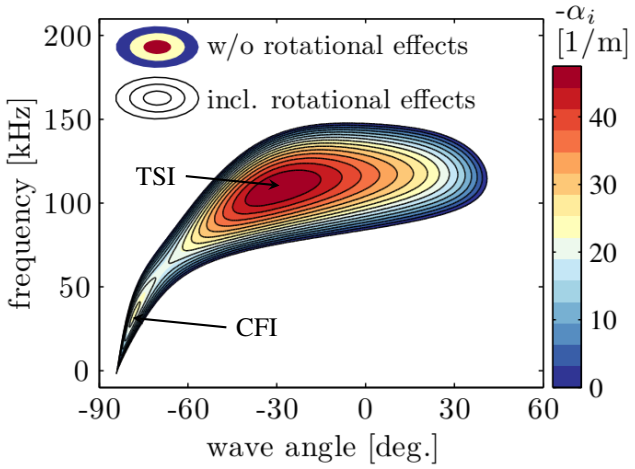

Fig. 8 Impact of rotational effects on the spatial growth rate, $-\alpha_i$, of a Tollmien-Schlichting and cross-flow instability at point S3; contours of the spatial growth rate in the $f - \Psi$ plane.

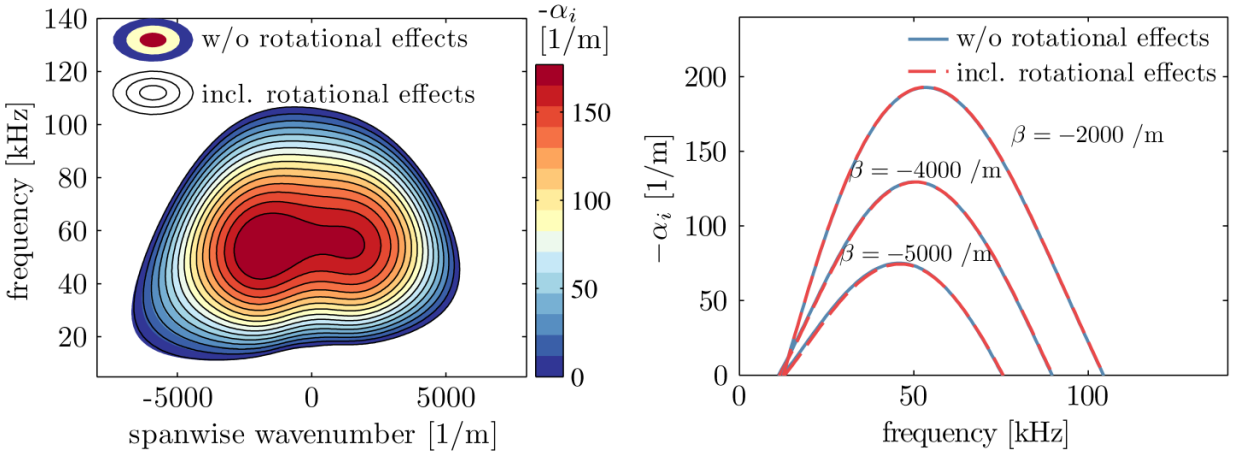

(a) **(b)**

Fig. 9 Impact of rotational effects on the spatial growth rate, $-\alpha_i$, of a Tollmien-Schlichting wave at point S_4; (a,b) as labeled in Fig. 5.

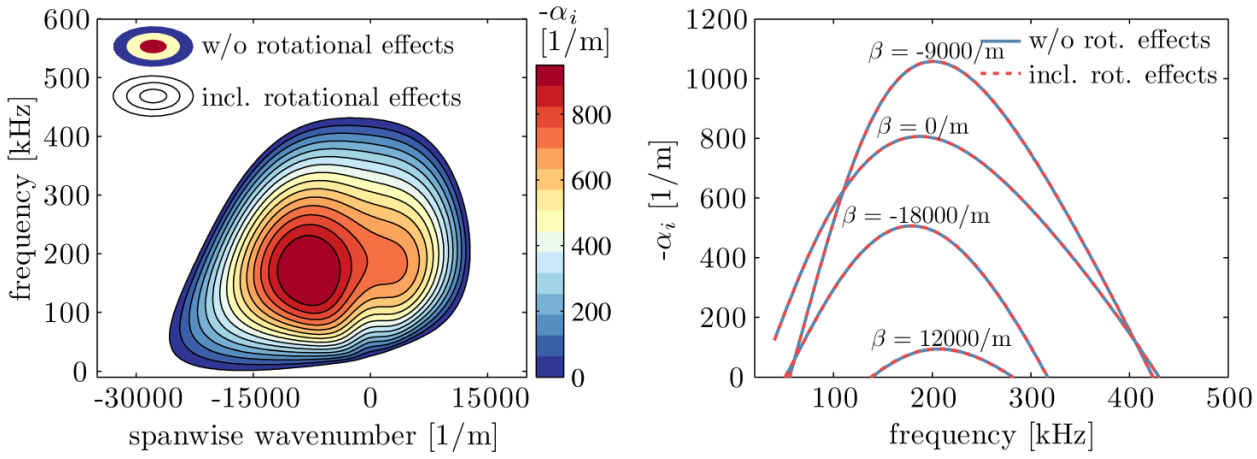

(a) **(b)**

Fig. 10 Impact of rotational effects on the spatial growth rate, $-\alpha_i$, of a Tollmien-Schlichting wave at point S_5; (a,b) as labeled in Fig. 5.

2. Rotor pressure side

Figures 11 and 12 depict the instability results for the two selected points on the rotor pressure side. The instability type at both locations is of a Tollmien-Schlichting wave. In accordance with the findings for the TSI on the suction side, rotation does not alter the instability characteristics here either.

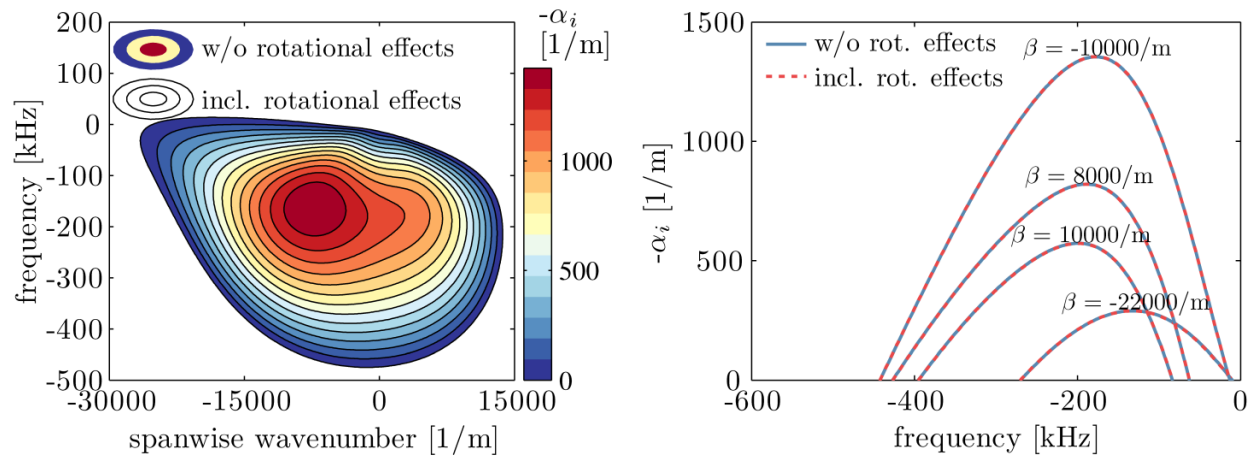

(a) **(b)**

Fig. 11 Impact of rotational effects on the spatial growth rate, $-\alpha_i$, of a Tollmien-Schlichting wave at point P_1; (a,b) as labeled in Fig. 5.

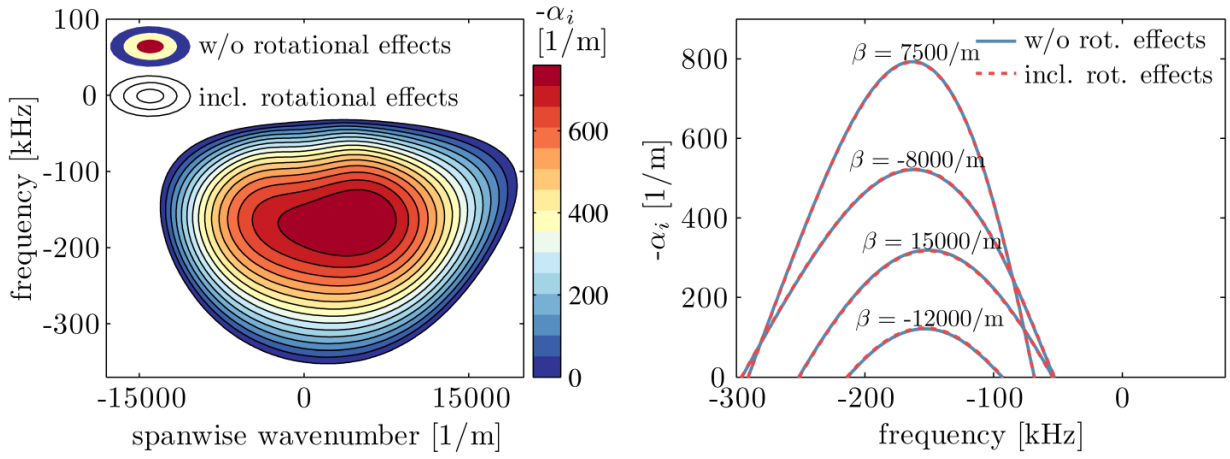

(a) **(b)**

Fig. 12 Impact of rotational effects on the spatial growth rate, $-\alpha_i$, of a Tollmien-Schlichting wave at point P_2; (a,b) as labeled in Fig. 5.

C. N-factor results for rotor suction side

So far, the investigations on the influence of the rotational terms on the instability properties of the primary modes were limited to selected local points on the rotor blade. To evaluate a more global effect and establish the link to transition prediction based on the e^N method, the local amplification rates are integrated into logarithmic amplification factors, the so-called N-factor.

The N-factor is defined as $N = \int_{s_0}^{s} \sigma \mathrm{d}s$, where s is the curvilinear abscissa along the considered line, and s_0 represents the location where the primary instability at a specific frequency and spanwise wavenumber is amplified for the first time. Note that the endpoint of the integration is restricted to the end of the laminar region at $x/x_{laminar} = 1$.

An overview of the maximum local amplification rate of the Tollmien-Schlichting instability on the rotor suction side and, for the sake of completeness, also on the pressure side is given in Fig. 13. The depicted growth rate corresponds to the maximum value determined over all frequencies and spanwise wavenumbers. The area with the highest amplification rates on the suction side is located in the hub region, where the largest adverse pressure gradient occurs (cf. Fig. 2). Thus, the highest N-factors are also to be expected there.

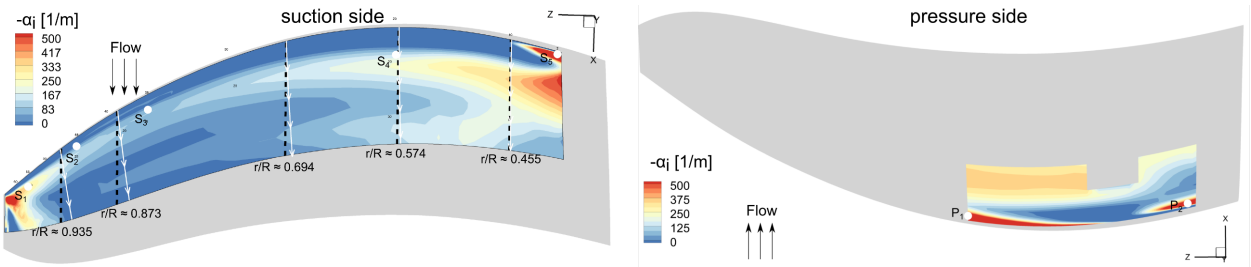

(a) **(b)**

Fig. 13 Isocontours of the maximum spatial growth rate ($-\alpha_i$) on (a) the rotor´s suction side and (b) its pressure side. The dashed black lines correspond to the N-factor integration path as used for the N-factor computation. The white lines denote the boundary-layer edge streamlines in the vicinity of the N-factor integration path.

The maximum N-factor value in three-dimensional flows, as present on the Z49 rotor, depends on the integration path, as well as the chosen N-factor integration strategy. The focus of this paper is on the impact of the rotational effects on the primary instability characteristics. Therefore, the most reasonable integration strategy is only of secondary interest, and line-in-flight cuts corresponding to isolines of the z-coordinate are used as integration paths, which are shown as dashed lines in Fig. 13(a). The white lines in Fig. 13(a) correspond to the boundary-layer edge streamlines in

the vicinity of the considered integration paths. It can be observed that the selected isolines in the lower rotor blade region correspond relatively well to the boundary-layer edge streamline, but the disparities increase with radius.

The prescribed-frequency/prescribed-spanwise-wavenumber integration strategy is used to compute the N-factors for both TSI and CFI. The envelope curve of all N-factors is thus defined as $N_{Envelope}(s) = \max_f \left(\max_\beta \left(N(s)\right)\right)$. An example of the streamwise evolution of a typical N-factor envelope curve, $N_{Envelope}$, is shown in Fig. 14(a).

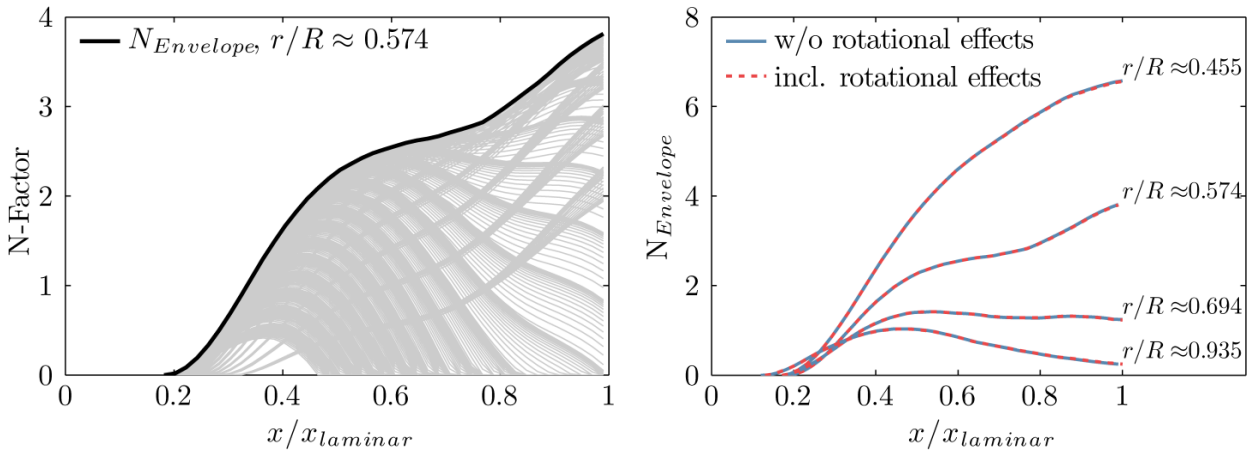

(a) **(b)**

Fig. 14 Streamwise evolution of (a) LST N-factors computed at various spanwise wavenumbers and frequencies and (b) LST T-S N-factor envelope curves integrated along paths with constant values of z (depicted in Fig. 13(a)).

In the following, the impact of the rotational terms on the streamwise evolution of the N-factor envelope curves is discussed separately for the two primary instabilities considered (TSI and CFI). Figure 14(b) shows the N-factor envelope curves for four different line-in-flight cuts for the T-S wave computed with LST. As indicated by the local results for points S_1, S_4, and S_5 and the spatial growth rate distribution on the rotor's suction side in Fig. 13, the N-factor for the integration path located the closest to the hub region ($r/R \approx 0.455$) reaches the highest value. As the distance from the axis of rotation increases, the maximum N-factor decreases. Thus, provided that the T-S wave amplitudes are sufficiently high enough, the laminar-turbulent transition is likely to first occur in the hub region. However, including the rotational effects in the LST has no impact on the transition scenario, since all curves shown in Fig. 14(b) coincide with the lines without rotational effects.

In addition to the LST analyses, selected PSE calculations were also performed for the cut at $r/R \approx 0.574$ with the spanwise wavenumber of $\beta = -900\,/\mathrm{m}$ (the value that leads to the highest LST N-factor in this cut). In contrast to the LST, the PSE also take nonlocal, nonparallel, and surface curvature effects into account. Figure 15(a) shows the comparison of the N-factors computed with LST and PSE for three selected frequencies. The N-factors curves calculated with PSE exhibit a similar evolution to those obtained with LST, but the nonlocal, nonparallel effects cause a slight increase of the maximum N-factor, at least for the higher frequencies investigated. The inclusion of the rotation effects in the PSE has no influence on the TSI-caused transition process since, as visible in Fig. 15(b), the curves are again on top of those without rotational effects.

Figure 16 depicts the N-factor envelope curve for the cross-flow instability in the cut at $r/R \approx 0.873$ computed with LST. When neglecting the rotational effects, the region of amplified CFI extends to $x/x_{laminar} = 0.22$. On the other hand, including the rotational effects in the instability analysis, the CFI is amplified throughout the considered section. Thus, the maximum N-factor significantly exceeds the value without rotational effects. However, the gain in CFI amplitude is still too low to trigger transition (e.g., a transition N-factor of 7.6 is given in Ref. [22]). A PSE analysis for this line did not reveal any amplified CFI, even when the rotational effects were included, which is likely due to the metric terms' stabilizing effect. Considering the metric terms in the LST also yields no amplified disturbances.

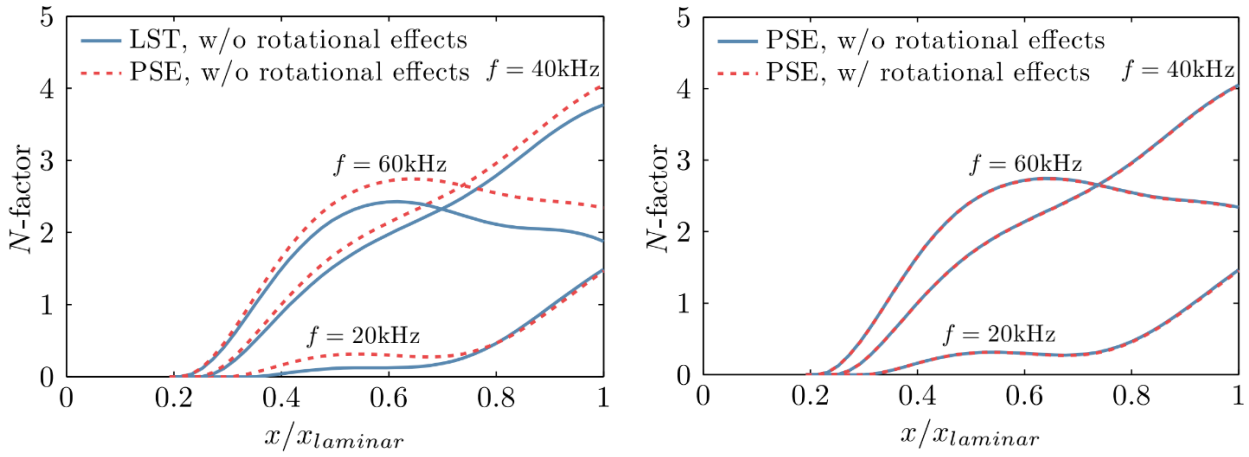

Fig. 15 Streamwise evolution of the N-factor at $r/R \approx 0.574$ for $\beta = -900$/m; (a) Comparison between LST and PSE N-factors; (b) Impact of rotation on the PSE N-factors.

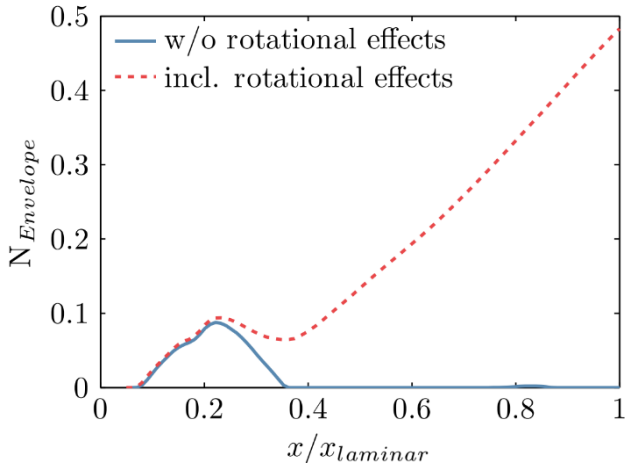

Fig. 16 Impact of the rotational effects on the streamwise evolution of the LST N-factor envelope curve for the cross-flow instability in the cut at $r/R \approx 0.873$.

VI. Conclusion

The impact of rotational terms appearing in a rotating reference frame (i.e., centrifugal and Coriolis accelerations) on the transition mechanisms for the Z49 rotor blade are investigated by means of linear stability computations. The effect of rotation is studied by comparing a set of instability computations accounting for rotational terms with a set of computations where those terms are neglected.

No new type of instability linked to the rotational terms is discovered. It is found that rotation solely alters the instability mechanisms already amplified on the rotor blade. Tollmien-Schlichting waves are found to be the dominant instability mechanism on the considered rotor geometry. Considering the rotational terms in the instability analysis hardly affects the T-S growth rates and N-factors obtained with local parallel theory (LST) or nonlocal nonparallel theory (PSE), independent from the distance to the rotation axis. Cross-flow instabilities (CFI) are found to be destabilized by the rotational effects, which is in accordance with previously published findings (see Ref. [19]). A possible reason for the differing effect of rotation on T-S waves and cross-flow instabilities is seen in the different wave propagation directions. Instabilities propagating transverse to the main flow direction (generally the CFI) are most strongly affected by rotation. This finding is consistent with results from the literature (see Refs. [17–19]). The N-factor for CFI increases when including the rotational terms in the instability analysis; however, the value is too low at the investigated operating condition ($N < 0.5$) to trigger transition on the Z49 rotor blade.

The results suggest that for an e^N-based transition prediction method in a rotating reference frame, the rotational terms do not necessarily have to be considered when T-S waves cause the transition. On the other hand, if cross-flow instabilities are the dominant transition mechanism, the terms should be included; otherwise, transition will be detected too far downstream.

The work of Dechamps & Hein [19] shows that the amplification rate of the rotation-affected instability increases with the number of revolutions per minute. Therefore, further investigations on the influence of the number of revolutions per minute are necessary to confirm this trend for industrially relevant geometries.

Acknowledgments

This project has received funding from the Clean Sky 2 Joint Undertaking (JU) under grant agreement No. 945583. The JU receives support from the European Union's Horizon 2020 research and innovation programme and the Clean Sky 2 JU members other than the Union. The support is gratefully acknowledged.

References

[1] McCroskey, W. J., "Measurements of Boundary Layer Transition, Separation and Streamline Direction on Rotating Blades," NASA TN D-6321, 1971.

[2] Schülein, E., Rosemann, H., and Schaber, S., "Transition Detection and Skin Friction Measurements on Rotating Propeller Blades," 28th AIAA Aerodynamic Measurement Technology, Ground Testing and Flight-Testing Conference, AIAA Paper 2012-3202, 2012, pp. 1–25. https://doi.org/10.2514/6.2012-3202

[3] Lang, W., Gardner, A. D., Mariappan, S., Klein, C., and Raffel, M., "Boundary-Layer Transition on a Rotor Blade Measured by Temperature Sensitive Paint, Thermal Imaging and Image Derotation," Experiments in Fluids, Vol. 56, No. 6, 2015, pp. 1–14. https://doi.org/10.1007/s00348-015-1988-5

[4] Himmelskamp, H., "Profile investigations on a rotating airscrew", MAP Völkenrode, Reports and Translations 832, 1947.

[5] Du, Z., Selig, M.S., "The effect of rotation on the boundary layer of a wind turbine blade", Renewable Energy, Vol. 20, No. 2, 2000, pp. 167–181. https://doi.org/10.1016/S0960-1481(99)00109-3

[6] Dumitrescu, H., Cardos, V., "Rotational effects on the boundary-layer flow in wind turbines", AIAA Journal, Vol. 42, No. 2, 2004, pp. 408–411. https://doi.org/10.2514/1.9103

[7] Menter, F. R., Langtry, R. B., Likki, S. R., Suzen, Y. B., Huang, P. G., and Völker, S. A., "A Correlation-Based Transition Model Using Local Variables—Part I: Model Formulation," Journal of Turbomachinery, Vol. 128, No. 3, 2004, pp. 413–422. https://doi.org/10.1115/1.2184352

[8] Weiss, A., Gardner, A. D., Schwermer, T., Klein, C., and Raffel, M., "On the Effect of Rotational Forces on Rotor Blade Boundary-Layer Transition," AIAA Journal, Vol. 57, No. 1, 2019, pp. 252–266. https://doi.org/10.2514/1.J057036

[9] Smith, A. M. O., and Gamberoni, N., "Transition, Pressure Gradient and Stability Theory," Douglas Aircraft Co. TR ES 26388, El Segundo, CA, Aug. 1956.

[10] Ingen, J. L. V., "A Suggested Semi-Empirical Method for the Calculation of the Boundary Layer Transition Region," Delft Univ. of Technology TR VTH-74, Delft, The Netherlands, Sept. 1956.

[11] Malik, M. R., Wilkinson, S. P., and Orszag, S. A., "Instability and Transition in Rotating Disk Flow," AIAA Journal, Vol. 19, No. 9, 1981, pp. 1131–1138. https://doi.org/10.2514/3.7849

[12] Hussain, Z., Garrett, S. J., and Stephen, S. O., "The Instability of the Boundary Layer over a Disk Rotating in an Enforced Axial Flow," Physics of Fluids, Vol. 23, No. 11, 2011, Paper 114108. https://doi.org/10.1063/1.3662133

[13] Garrett, S. J., Hussain, Z., and Stephen, S. O., "Boundary-Layer Transition on Broad Cones Rotating in an Imposed Axial Flow," AIAA Journal, Vol. 48, No. 6, 2010, pp. 1184–1194. https://doi.org/10.2514/1.J050021

[14] Potter. C., and Chawla, M. D., "Stability of Boundary Layer Flow Subject to Rotation," Physics of Fluids, Vol. 14, No. 11, 1971, pp. 2278–2281. https://doi.org/10.1063/1.1693328

[15] Gross, A., Fasel, H. F., Friederich, T., and Kloker, M. J., "Numerical Investigation of S822 Wind Turbine Airfoil," 40th Fluid Dynamics Conference and Exhibit, AIAA Paper 2010-4478, 2010. https://doi.org/10.2514/6.2010-4478

[16] Martinez Hernandez, G. G., Sørensen, J. N., and Shen, W. Z., "Laminar-Turbulent Transition on Wind Turbines," Ph.D. Thesis, Technical Univ. of Denmark, Kongens Lyngby, Denmark, 2012.

[17] Pascal, L., Barrier, R., Billonet, G., and Marty, J., "Linear Stability Analysis in Rotating Frames for Fan Blade Transition Prediction," AIAA Journal, Vol. 58, No. 8, 2020, pp. 3264–3271. https://doi.org/10.2514/1.J059101

[18] Yecko, P., Rossi, M., "Transient growth and instability in rotating boundary layers", Phys. Fluids, Vol. 16, No. 7, 2004, pp. 2322–2335. https://doi.org/10.1063/1.1737391

[19] Dechamps, X., and Hein, S., "Extension of the PSE Code NOLOT for Transition Analysis in Rotating Reference Frames," New Results in Numerical and Experimental Fluid Mechanics XI: Contributions to the 20th STAB/DGLR Symposium, Vol. 136, Springer, Brunswick, Germany, 2017, pp. 179–188. https://doi.org/10.1007/978-3-319-64519-3_16

[20] Hein, S., Bertolotti, F., Simen, M., Hanifi, A., Henningson, D.: Linear non-local instability analysis - The linear NOLOT code, DLR IB 223-94 A56, 1995.

[21] Brazier, J.-P., "MAMOUT: Modules d'Analyse MOdale Unidimensionnelle avec les Polynômes de Tchebychev. Instructions Pour l'Emploi des Programmes Spectre et Moditer Version 6," ONERA TR RT 1/24067 DMAE, Toulouse, France, 2015.

[22] Kruse, M., Muñoz, F., and Radespiel, R., "Transition Prediction Results for Sickle Wing and NLF(1)-0416 Test Cases," 2018 AIAA Aerospace Sciences Meeting, AIAA Paper 2018-0537, 2018. https://doi.org/10.2514/6.2018-0537